

Article

## A High Step-Down Interleaved Buck Converter with Active-Clamp Circuits for Wind Turbines

Cheng-Tao Tsai <sup>1</sup> and Chih-Lung Shen <sup>2,\*</sup>

<sup>1</sup> Department of Electrical Engineering, National Chin-Yi University of Technology, Taichung 41170, Taiwan; E-Mail: cttsai@ncut.edu.tw

<sup>2</sup> Department of Electronic Engineering, National Kaohsiung First University of Science and Technology, Kaohsiung 824, Taiwan

\* Author to whom correspondence should be addressed; E-Mail: clshen@ccms.nkfust.edu.tw; Tel.: +886-7-6011000 (ext. 2515); Fax: +886-7-6011386.

Received: 30 August 2012; in revised form: 17 November 2012 / Accepted: 26 November 2012 /

Published: 6 December 2012

---

**Abstract:** In this paper, a high step-down interleaved buck coupled-inductor converter (IBCC) with active-clamp circuits for wind energy conversion has been studied. In high step-down voltage applications, an IBCC can extend duty ratio and reduce voltage stresses on active switches. In order to reduce switching losses of active switches to improve conversion efficiency, a IBCC with soft-switching techniques is usually required. Compared with passive-clamp circuits, the IBCC with active-clamp circuits have lower switching losses and minimum ringing voltage of the active switches. Thus, the proposed IBCC with active-clamp circuits for wind energy conversion can significantly increase conversion efficiency. Finally, a 240 W prototype of the proposed IBCC with active-clamp circuits was built and implemented. Experimental results have shown that efficiency can reach as high as 91%. The proposed IBCC with active-clamp circuits is presented in high step-down voltage applications to verify the performance and the feasibility for energy conversion of wind turbines.

**Keywords:** high-step; coupled-inductor; passive-clamp; active-clamp; soft-switching

---

## 1. Introduction

Limited fossil energy and serious greenhouse effect have forced most engineers to research renewable energy sources. The typical renewable energy sources include solar, wind and geothermal energy, which have the features of cleanliness, freedom from maintenance and abundance [1]. Therefore, the development of renewable and clean energy sources to substitute for fossil fuels has been an important topic. Currently, wind is one of most widely utilized renewable energies. The wind turbine technology has been undergoing a dramatic development and now is the world's fastest growing energy form [2]. However, due to the instability and intermittent characteristics of wind energy, it cannot provide a constant or stable power output. Thus, the power processor usually adopts a dc/dc converter as its energy processing system [2–4].

In wind energy conversion, most dc/dc converters are usually provided a low output voltage ( $24 V_{dc}$  or  $12 V_{dc}$ ) and high output current to load. Therefore, a conventional interleaved buck converter (IBC) as shown in Figure 1 is widely adopted, because it has a simple structure, high output current density and low output current ripple. However, in high step-down voltage applications, it suffers from extremely short duty ratio and high component stresses, resulting in low conversion efficiency [5–8]. To alleviate these limitations, the IBCC is proposed, as shown in Figure 2 (where  $n_1$  and  $n_{11}$  are primary and secondary winding turns of coupled inductor  $L_1$ ,  $n_2$  and  $n_{22}$  are primary and secondary winding turns of coupled inductor  $L_2$ ). A coupled inductor has a simple winding structure, and it can extend duty ratio and reduce peak primary winding current. Thus, a coupled inductor based on converter is relatively attractive. Although the IBCC can yield high step-down voltage ratios, its leakage inductance ( $L_{k1}$  and  $L_{k2}$ ) of coupled inductors not only increases voltage stresses on the active switches but induces significant switching losses too. To overcome these problems, the IBCC with passive-clamp circuits, as shown in Figure 3, it can recover the leakage energy and reduce voltage stresses of active switches, but the active switches are still operated in a hard-switching manner during turn-on transition [9–12].

**Figure 1.** Topology of conventional IBC for wind turbine applications.

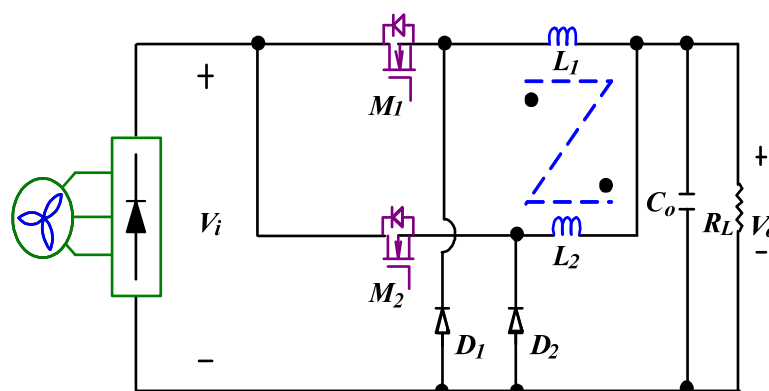


Figure 2. Topology of the IBCC for wind turbine applications.

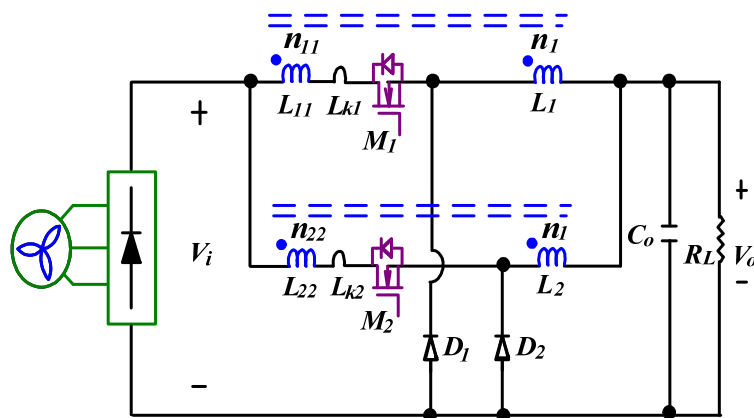
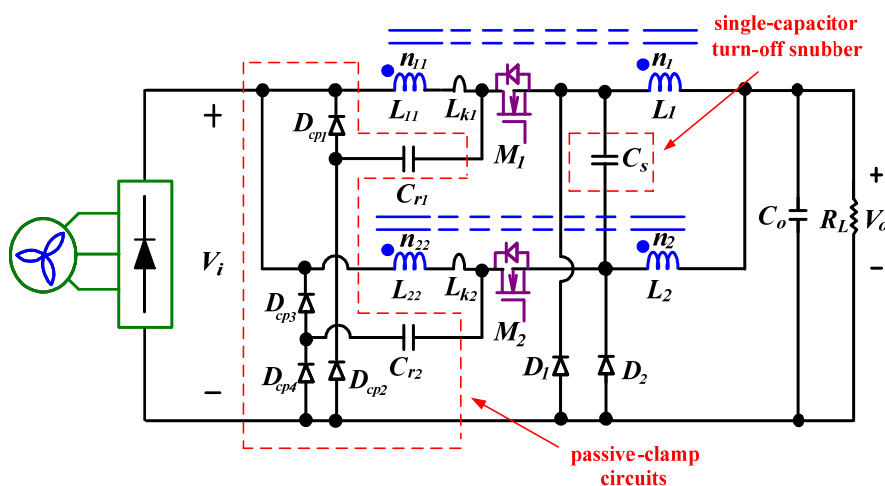
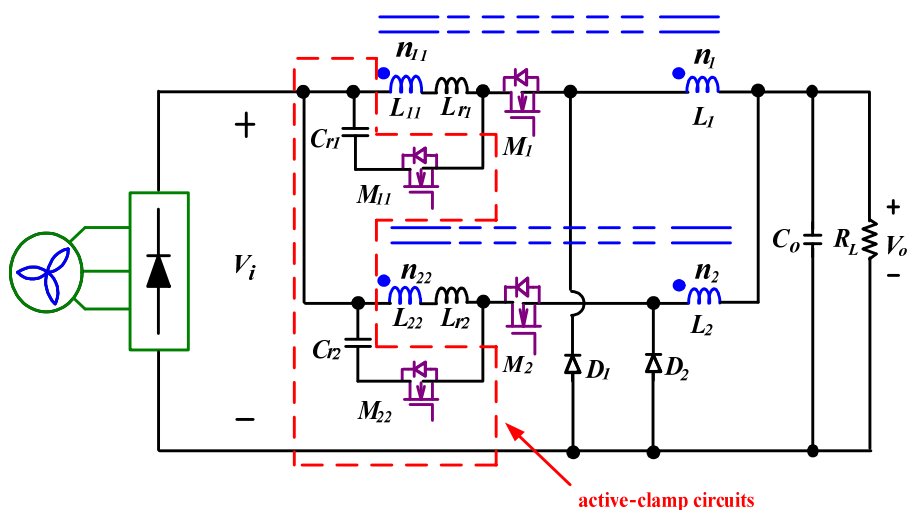


Figure 3. Topology of IBCC with passive-clamp circuits for wind turbine applications.



In this paper, the IBCC with active-clamp circuits is proposed, as shown in Figure 4. The active-clamp circuits can implement zero-voltage switching (ZVS) of active switches during turn-on transition and recycle the energy trapped in leakage inductance of coupled inductors.

Figure 4. Topology of IBCC with active-clamp circuits for wind turbine applications.



Therefore, the conversion efficiency can be improved significantly. In Figure 4, to achieve a zero-voltage switching (ZVS) feature at turn-on transition for both main switches ( $M_1$  and  $M_2$ ) and auxiliary switches ( $M_{11}$  and  $M_{22}$ ), the extra resonant inductors ( $L_{r1}$  and  $L_{r2}$ ) are usually required. In particular, the resonant inductors can also limit the rate of decrease of the free-wheeling diode currents at turn-off transition, reducing reverse-recovery losses a lot and further improving conversion efficiency [13–18].

### 2. Selection of Active-Clamp Circuit

The active-clamp circuits discussed in this study can be selected as two circuits, in which one is a flyback-type clamp circuit, as shown in Figure 5, and the other is a boost-type clamp circuit, as shown in Figure 6.

**Figure 5.** Topology of IBCC with flyback-type active-clamp circuit.

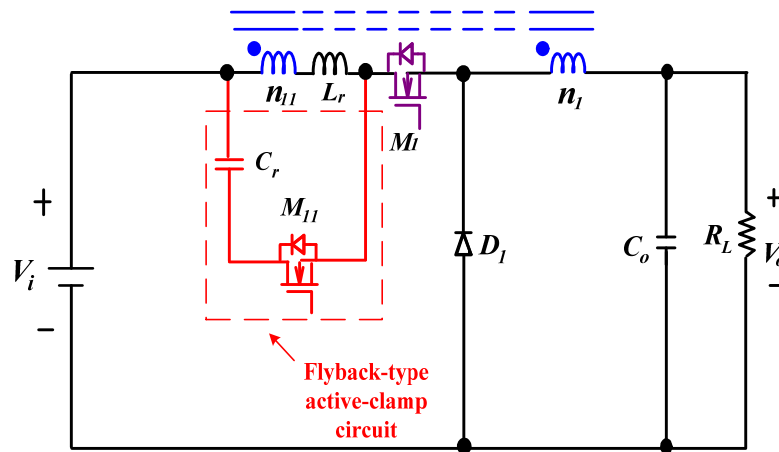
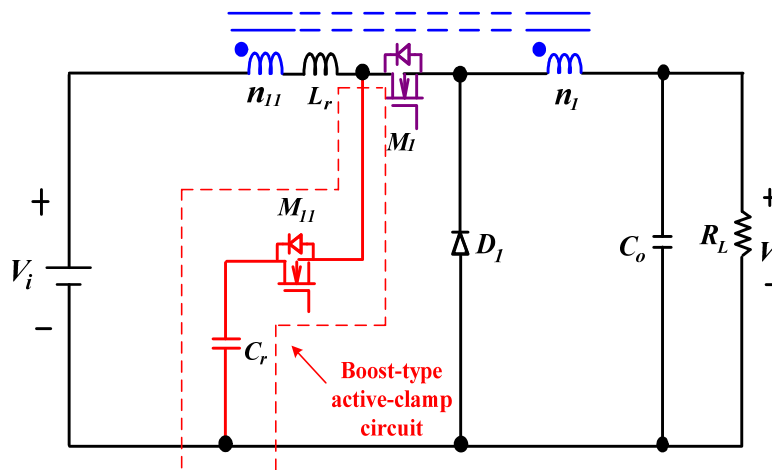


**Figure 6.** Topology of IBCC with boost-type active-clamp circuit.



In Figure 5, by volt-second balance law, the voltage of the clamp capacitor  $V_{cr(flyback)}$  can be expressed as:

$$V_{cr(flyback)} = V_i \frac{D}{1-D} \tag{1}$$

where  $V_i$  is input voltage and  $D$  is duty ratio of main switch  $M_1$ . Similarly, In Figure 6, the voltage of the clamp capacitor  $V_{cr(boost)}$  can be expressed as:

$$V_{cr(boost)} = V_i \frac{1}{1 - D} \tag{2}$$

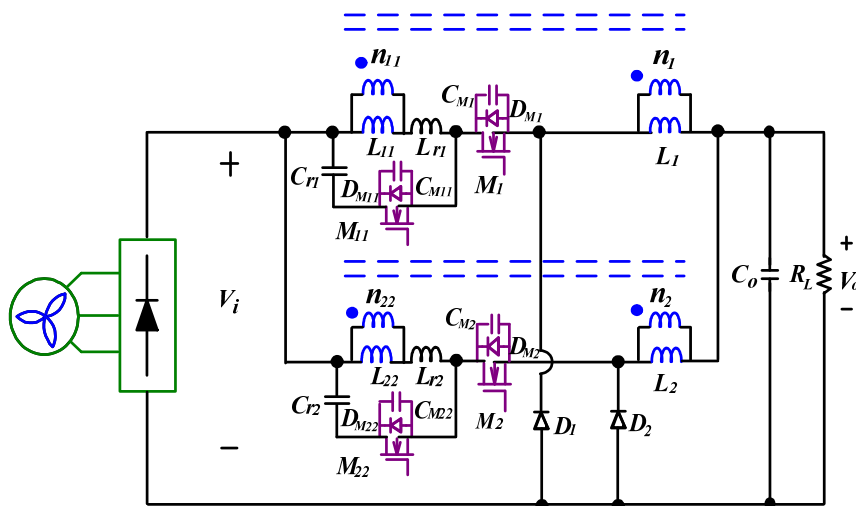
From Equations (1) and (2), we can see that voltage stress of the flyback-type clamp circuit is less than that of the boost-type one, making the flyback-type clamp circuit more attractive. In this study, only the flyback-type clamp is considered due to its obvious advantages. Thus, the IBCC with flyback-type clamp circuits, as shown in Figure 4, is proposed.

### 3. Operational Principle

The proposed IBCC (Figure 4) mainly includes two sets of coupled inductors  $L_1, L_2$ , main switches  $M_1, M_2$ , auxiliary switches  $M_{11}, M_{22}$ , resonant inductors  $L_{r1}, L_{r2}$ , clamp capacitors  $C_{r1}, C_{r2}$  and free-wheeling diodes  $D_1, D_2$ . In order to analyze the ZVS feature of the main and auxiliary switches ( $M_1, M_2, M_{11}$  and  $M_{22}$ ), their stray capacitors ( $C_{M1}, C_{M2}, C_{M11}$  and  $C_{M22}$ ) will be considered at the steady-state operation of the circuit, as shown in Figure 7. In Figure 7, each set of the coupled inductors can be treated as a transformer with two magnetizing inductors. Its turns ratio is defined as:

$$n = \frac{(n_1 + n_{11})}{n_1} = \frac{(n_2 + n_{22})}{n_2}, \quad (n \geq 1) \tag{3}$$

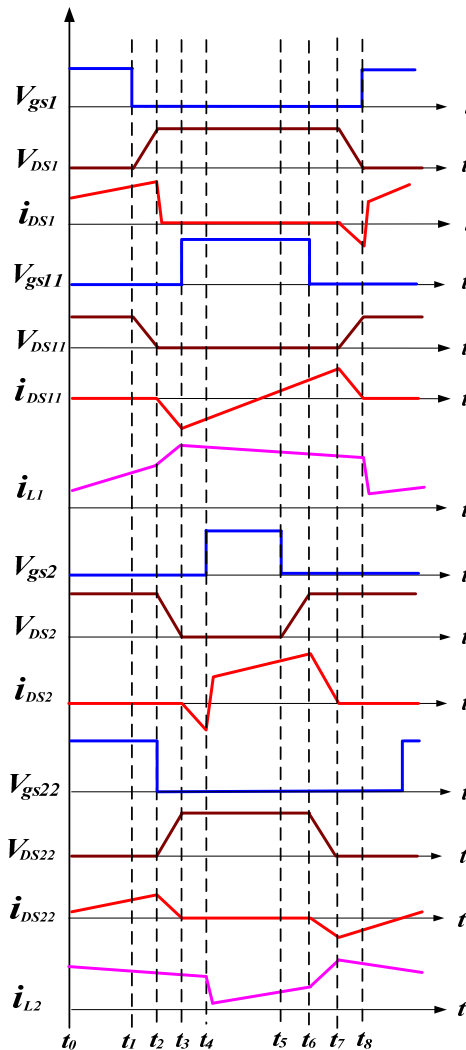
**Figure 7.** The proposed IBCC with active-clamp circuits for wind turbine applications.



The following assumptions are made over one switching cycle:

- (1) clamp capacitors  $C_{r1}, C_{r2}$  and output filter capacitor  $C_o$  are large enough so that the voltages across them are constant over a switching period,
- (2) winding and turns of coupled inductors ( $L_1$  and  $L_2$ ) are identical, and
- (3) all semiconductor components are ideal, except the MOSFETs ( $M_1, M_2, M_{11}$  and  $M_{22}$ ).

Figure 8. Key waveforms of the IBCC with active-clamp circuits.



Under continuous inductor current operation, eight major operating modes are identified over one switching cycle. Figure 8 shows conceptual voltage and current waveforms of its key components and Figure 9 shows equivalent circuits of its operational modes:

Mode 1 [Figure 9(a),  $t_0 \leq t < t_1$ ]:

In this mode, main switch  $M_1$  and auxiliary switch  $M_{22}$  are turned on. Inductor current  $i_{L1}$  flowing through the path  $V_i$ - $L_{11}$ - $L_{r1}$ - $M_1$ - $L_1$  to the load is linearly increased. Clamping capacitor  $C_{r2}$  begins releasing its stored energy by coupled-inductor  $L_2$  and  $L_{22}$  transferring to the load.

Mode 2 [Figure 9(b),  $t_1 \leq t < t_2$ ]:

At time  $t = t_1$ , main switch  $M_1$  is turned off, resonant inductor  $L_{r1}$  releases energy to stray capacitance  $C_{M1}$  of  $M_1$  and stray capacitance  $C_{M11}$  of  $M_{11}$  with a resonant manner. When time  $t = t_2$ , stray capacitance  $C_{M1}$  of  $M_1$  will be charged toward to  $(V_i + nV_o)$  while stray capacitance  $C_{M11}$  of  $M_{11}$  will be discharged down to zero. To achieve a ZVS feature for auxiliary switch  $M_{11}$ , the energy stored in resonant inductor  $L_{r1}$  should satisfy the following inequality:

$$0.5 \times [i_{DS1}(t_1)]^2 L_{r1} \geq 0.5 \times [V_{DS11}(t_1)]^2 (C_{M1} // C_{M11}) \tag{4}$$

**Figure 9.** Equivalent circuit modes of the IBCC with active-clamp circuits operating over one switching cycle. (a) Mode 1 [ $t_0 \leq t < t_1$ ]; (b) Mode 2 [ $t_1 \leq t < t_2$ ]; (c) Mode 3 [ $t_2 \leq t < t_3$ ]; (d) Mode 4 [ $t_3 \leq t < t_4$ ]; (e) Mode 5 [ $t_4 \leq t < t_5$ ]; (f) Mode 6 [ $t_5 \leq t < t_6$ ]; (g) Mode 7 [ $t_6 \leq t < t_7$ ]; (h) Mode 7 [ $t_7 \leq t < t_8$ ].

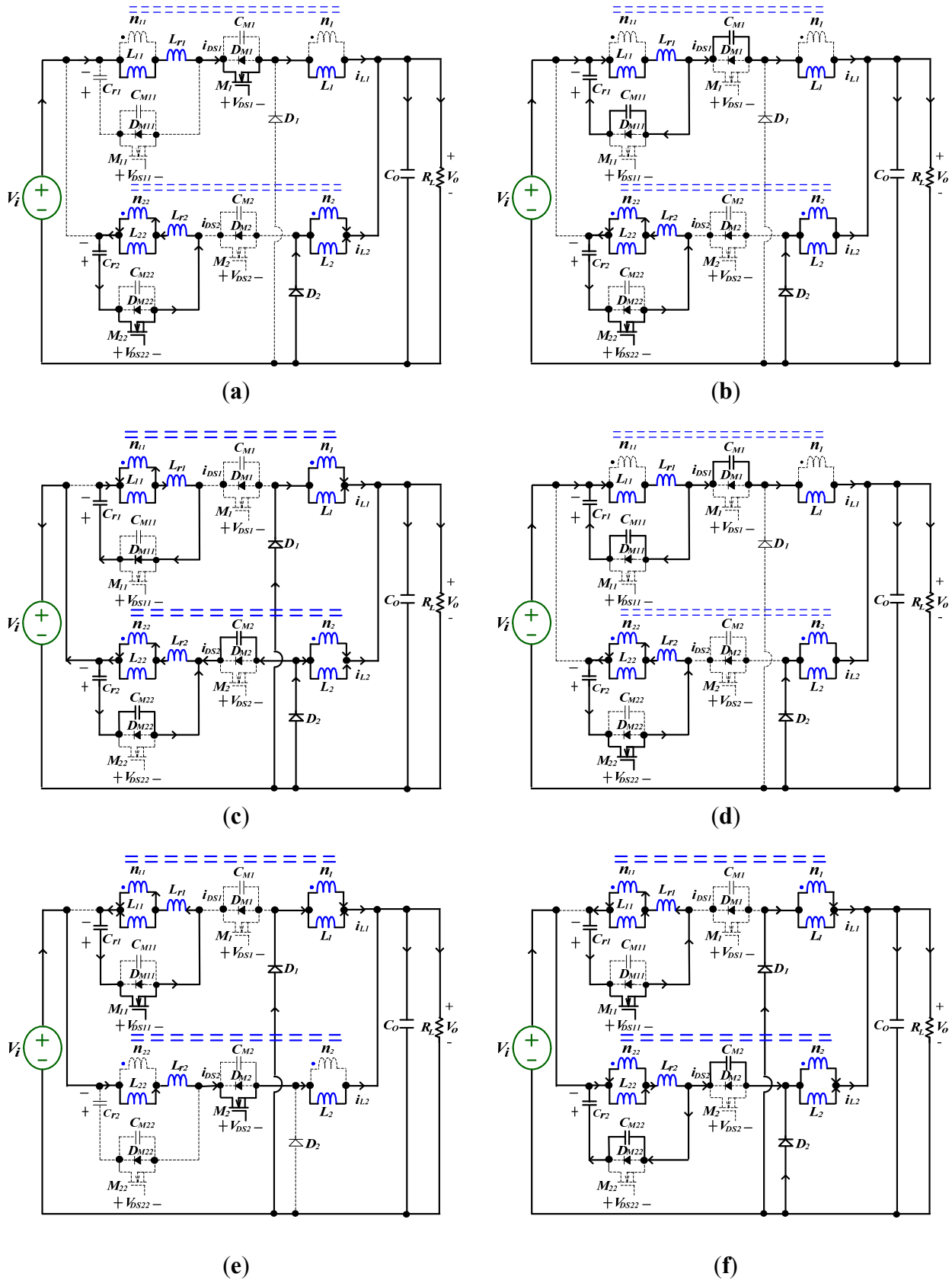
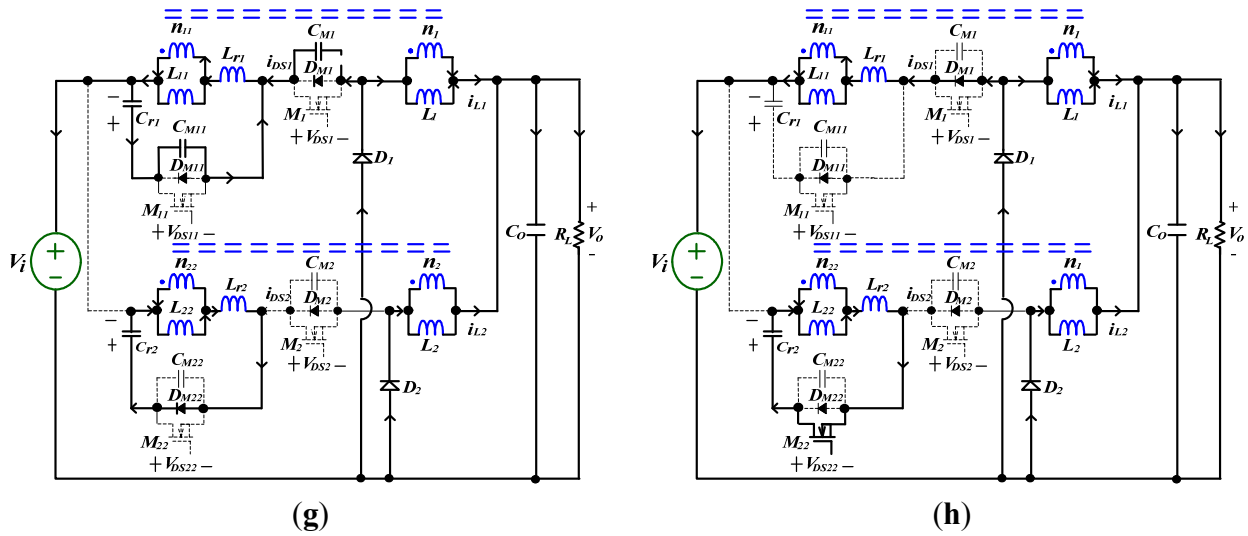


Figure 9. Cont.



Mode 3 [Figure 9(c),  $t_2 \leq t < t_3$ ]:

At time  $t = t_2$ , voltage  $V_{DS11}$  of  $M_{11}$  is dropped to zero and  $V_{DS1}$  of  $M_1$  is reached to  $V_i + nV_o$ . Main switch  $M_1$  is turned off and free-wheeling diode  $D_1$  is turned on. Current  $i_{DS11}$  forces the body diode  $D_{M11}$  of  $M_{11}$  conducting to create a ZVS operation for  $M_{11}$ . In this mode, inductor current  $i_{L1}$  begins decreased through free-wheeling diode  $D_1$  to the load. The inductor currents  $i_{L1}$  and  $i_{L2}$  can be expressed as follows:

$$i_{L1}(t) = \frac{V_o}{nL_1} \times (t - t_2) + i_{L1}(t_2) \tag{5}$$

and:

$$i_{L2}(t) = \frac{V_o}{nL_2} \times (t - t_2) + i_{L2}(t_2) \tag{6}$$

During this interval, the energy trapped in the resonant inductor  $L_{r1}$  is recycled to clamp capacitor  $C_{r1}$ . Due to the clamp capacitance of  $C_{r1}$  being large enough, voltage  $V_{Cr1}$  will keep constant.

When auxiliary switch  $M_{22}$  is turned off at time  $t_2$ , resonant inductor  $L_{r2}$  resonates with  $C_{M2}$  and  $C_{M22}$ . Stray capacitance  $C_{M22}$  of  $M_{22}$  will be charged toward to  $V_{Cr2} + [n/(1 + n)](V_i - V_o)$ , while stray capacitance  $C_{M2}$  of  $M_2$  will be discharged down to zero. To achieve a ZVS feature for main switch  $M_2$ , the energy trapped in resonant inductor  $L_{r2}$  should satisfy the following inequality:

$$0.5 \times [i_{DS2}(t_2)]^2 L_{r2} \geq 0.5 \times [V_{DS2}(t_2)]^2 (C_{M2} // C_{M22}) \tag{7}$$

Mode 4 [Figure 9(d),  $t_3 \leq t < t_4$ ]:

At time  $t = t_3$ , auxiliary switch  $M_{11}$  is turned on under ZVS condition. When voltage  $V_{DS2}$  of  $M_2$  is dropped to zero and  $V_{DS22}$  of  $M_{22}$  is reached to  $V_{Cr2} + [n/(1 + n)](V_i - V_o)$ , auxiliary switch  $M_{22}$  is turned off and current  $i_{DS2}$  forces the body diode  $D_{M2}$  of  $M_2$  conducting to create a ZVS operation for  $M_2$ . In this mode, inductor current  $i_{L1}$  and  $i_{L2}$  are continuously decreased through free-wheeling diode  $D_1$  and  $D_2$  to the load.

Mode 5 [Figure 9(e),  $t_4 \leq t < t_5$ ]:

At time  $t = t_4$ , main switch  $M_2$  is turned on under ZVS condition and free-wheeling diode  $D_2$  is turned off. Inductor current  $i_{L2}$  flowing through the path of  $V_i$ - $L_{22}$ - $L_{r2}$ - $M_2$ - $L_2$  to the load is linearly increased, and inductor current  $i_{L1}$  continuously flowing through the path of  $V_o$ - $D_1$ - $L_1$  is linearly decreases, which can be expressed as follows:

$$i_{L1}(t) = \frac{V_o}{nL_1} \times (t - t_4) + i_{L1}(t_4) \quad (8)$$

and:

$$i_{L2}(t) = \frac{V_o}{nL_2} \times (t - t_4) + i_{L2}(t_4) \quad (9)$$

Mode 6 [Figure 9(f),  $t_5 \leq t < t_6$ ]:

At time  $t = t_5$ , main switch  $M_2$  is turned off, resonant inductor  $L_{r2}$  releases energy to stray capacitance  $C_{M2}$  of  $M_2$  and stray capacitance  $C_{M22}$  of  $M_{22}$  with a resonant manner. When time  $t = t_6$ , the stray capacitance  $C_{M2}$  will be charged toward to  $(V_i + nV_o)$ , while stray capacitance  $C_{M22}$  will be discharged to zero. To achieve a ZVS feature for main switch  $M_{22}$ , the energy stored in resonant inductor  $L_{r2}$  should satisfy the following inequality:

$$0.5 \times [i_{DS2}(t_5)]^2 L_{r2} \geq 0.5 \times [V_{DS22}(t_5)]^2 (C_{M2} // C_{M22}) \quad (10)$$

Mode 7 [Figure 9(g),  $t_6 \leq t < t_7$ ]:

At time  $t = t_6$ , voltage  $V_{DS22}$  of  $M_{22}$  is dropped to zero and voltage  $V_{DS2}$  of  $M_2$  is reached to  $(V_i + nV_o)$ , main switch  $M_2$  is turned off and free-wheeling diode  $D_2$  is conducted. Current  $i_{DS22}$  forces the body diode  $D_{M22}$  of  $M_{22}$  conducting and to create a ZVS operation for auxiliary switch  $M_{22}$ . In this mode, inductor current  $i_{L2}$  begins decreased through free-wheeling diode  $D_2$  to the load. The inductor currents  $i_{L1}$  and  $i_{L2}$  can be expressed as follows:

$$i_{L1}(t) = \frac{V_o}{nL_1} \times (t - t_6) + i_{L1}(t_6) \quad (11)$$

and:

$$i_{L2}(t) = \frac{V_o}{nL_2} \times (t - t_6) + i_{L2}(t_6) \quad (12)$$

The energy trapped in the resonant inductor  $L_{r2}$  is recycled to clamp capacitor  $C_{r2}$ . Since the clamping capacitor of  $C_{r2}$  is large enough, voltage  $V_{cr2}$  will keep constant.

Mode 8 [Figure 9(h),  $t_7 \leq t < t_8$ ]:

At time  $t = t_7$ , voltage  $V_{DS1}$  of  $M_1$  is dropped to zero and voltage  $V_{DS11}$  of  $M_1$  is reached to  $(V_i + nV_o)$ , main switch  $M_{11}$  is turned off. Current  $i_{DS1}$  forces the body diode  $D_{M1}$  of  $M_1$  conducting and to create a ZVS operation for main switch  $M_1$ . When main switch  $M_1$  starts conducting again at the end of mode 8, the converter operation over one switching cycle is completed.

### 4. Feature Analysis

The proposed IBCC with active-clamp circuits can extend duty ratio of the active switches and reduce component stress. This section describes the feature analysis and efficiency estimation for the proposed IBCC. The feature analysis includes voltage gain, duty ratio, and voltage stress of free-wheeling diode:

#### 4.1. Voltage Gain and Duty Ratio

From the key waveforms of the converter shown in Figure 8 and by applying the volt-second balance law, the voltage gain and duty ratio can be derived as:

$$\frac{V_o}{V_i} = \frac{D}{D + n(1 - D)}, \quad (n \geq 1) \tag{13}$$

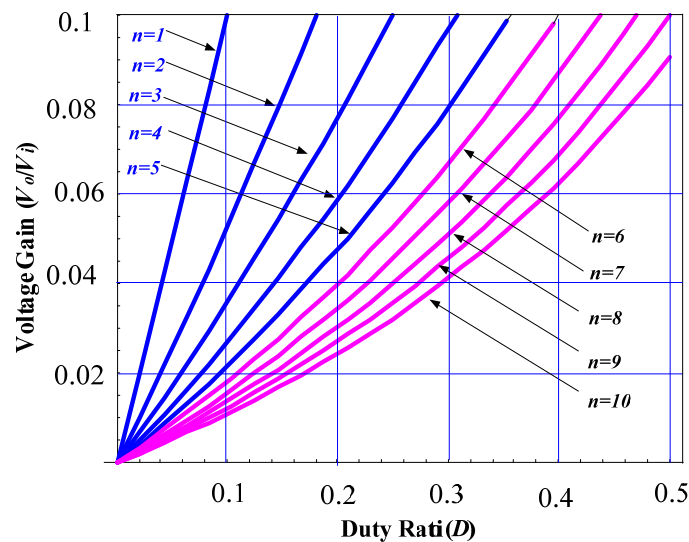
and:

$$D = \frac{nV_o}{V_i + nV_o - V_o}, \quad (D < 0.5) \tag{14}$$

where  $D$  is the duty ratio of the main switch ( $M_1$  or  $M_2$ ), respectively.

For example, input voltage  $V_i = 150\text{--}250 \text{ V}_{dc}$  and output voltage  $V_o = 12 \text{ V}_{dc}$  are considered. From Equations (13) and (14), we can sketch a set of curves showing the relationship between duty ratio  $D$  and voltage gain of  $V_o/V_i$  for different values of turns ratio  $n$ , as illustrated in Figure 10.

**Figure 10.** Plots of  $V_o/V_i$  versus duty ratio  $D$ .



#### 4.2. Voltage Stress of Free-Wheeling Diode and Active Switch

According to description of Mode 2, the voltage stress of the free-wheeling diodes ( $D_1$  and  $D_2$ ) and active switches ( $M_1$  and  $M_2$ ) can be derived as:

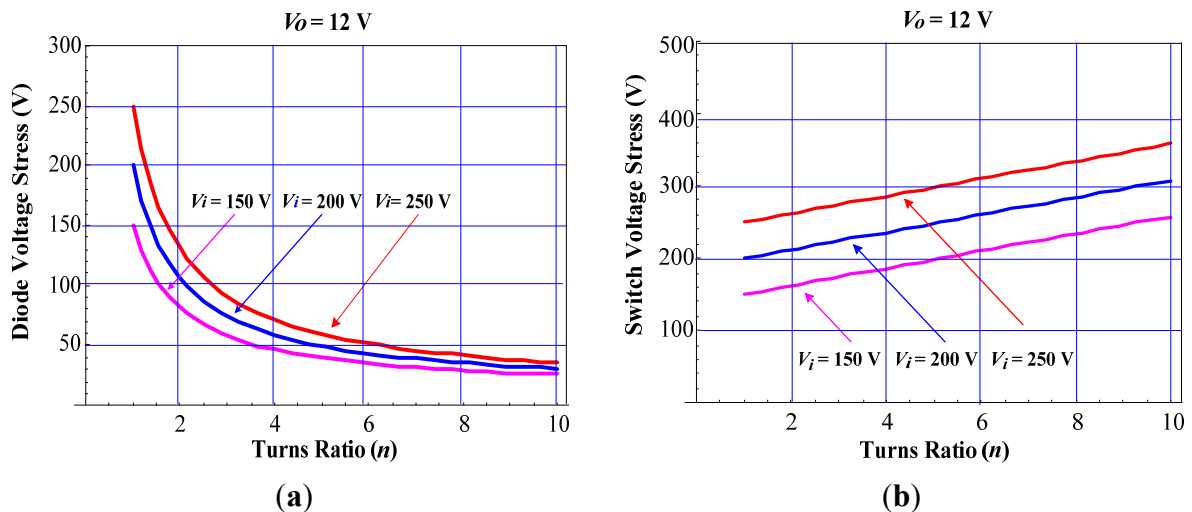
$$V_D = V_{D1} = V_{D2} = \frac{(V_i - V_o)}{n} + V_o \tag{15}$$

and

$$V_{DS} = V_{DS1} = V_{DS2} = V_i + (n - 1)V_o \tag{16}$$

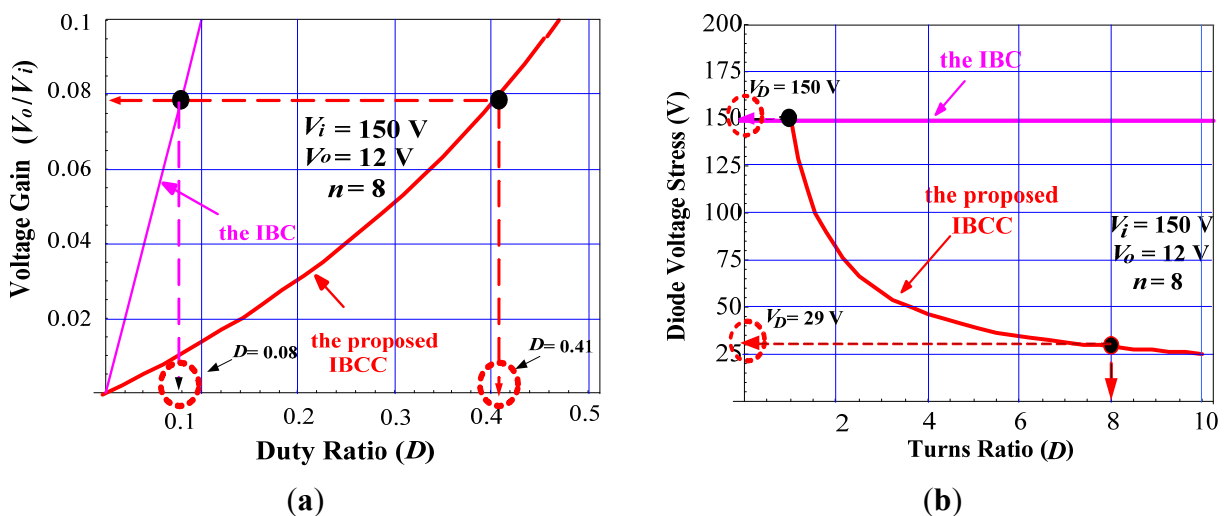
From Equations (15) and (16), we can sketch a set of curves showing the free-wheeling diode voltage stress *versus* turns ratio  $n$  under different input voltages, as shown in Figure 11.

**Figure 11.** Plots of voltage stress *versus* turns ratio  $n$  of the coupled inductor. (a) free-wheeling diodes ( $D_1$  and  $D_2$ ); (b) active switches ( $M_1$  and  $M_2$ ).



To objectively judge the merits of the proposed converter, performance comparison between the proposed converter and the IBC is shown in Figure 12. From these plots, it can be seen that the proposed IBCC yields higher duty ratio and lower diode voltage stress over the IBC.

**Figure 12.** Performance comparison between the IBCC and the IBC. (a) Duty ratio; (b) voltage stress of the free-wheeling diode.



## 5. Power Losses Estimation and Experimental Results

To verify the performance of the proposed IBCC with active-clamp circuits is higher than that of the IBCC with passive-clamp circuits, a 240 W prototype of the proposed converter was designed and built, as shown in Figure 7. Its specifications are listed as follows:

- Input voltage: 150–200 V<sub>dc</sub>;
- Output voltage: 12 V<sub>dc</sub>;
- Maximum output current: 20 A;
- Switching frequency: 75 kHz.

As followed are the design considerations, power losses estimation and experimental results for the proposed IBCC with active-clamp circuits.

### 5.1. Design Considerations of Key Components

A larger duty ratio  $D$  corresponds to a larger coupled-inductor turns ratio  $n$ , which results in a lower voltage stress on free-wheeling diodes  $D_1$  and  $D_2$ . In order to accommodate variations of loads, a proper turns ratio  $n$  of the coupled inductors is needed. From Figure 10, we can obtain a proper coupled-inductor turns ratio  $n = 8$ . Its maximum duty ratio is  $D_{max} \approx 0.41$  under input voltage  $V_i = 150$  V<sub>dc</sub> and minimum duty ratio is  $D_{min} \approx 0.34$  under input voltage  $V_i = 200$  V<sub>dc</sub>.

#### 5.1.1. Design of the Coupled Inductors

Once the coupled-inductor turns ratio  $n = 8$  is selected, the maximum duty ratio can be determined as  $D_{max} \approx 0.41$ . The maximum current ripple of the coupled inductors is designed with  $i_{L(ripple)} = i_{L1(ripple)} = i_{L2(ripple)} = 10$  A, and coupled inductance  $L = L_1 = L_2$  can be determined as:

$$L = \frac{(V_{i(\min)} - V_o)D_{\max}}{n^2 i_{L(ripple)} f_s} = \frac{(150 - 12)0.41}{64 \times 10 \times 75 \times 10^3} = 1.2 \mu\text{H} \quad (17)$$

where  $f_s$  is the switching frequency of the active switches. Coupled inductance  $L = 3 \mu\text{H}$  is selected in the design. When the turns ratio  $n = (n_1 + n_2)/n_1$  is equal to 8, the coupled inductance  $L_{11} = L_{22}$  can be determined as:

$$L_{11} = L_{22} = (n - 1)^2 L = 7^2 \times 3 \mu = 147 \mu\text{H} \quad (18)$$

From TDK datasheets, we choose an optimum ferrite material PC40 and maximum flux  $B_{max} = 200$  mT, maximum winding factor  $K_{w(max)} = 0.4$  and maximum current density  $J_{max} = 400$  A/cm<sup>2</sup>. Thus, the area product of the core can be determined as:

$$A_p = W_a A_e > \frac{(P_o + \frac{P_o}{\eta}) \times 10^4}{B_{\max} K_{w(max)} J_{\max} f_s} = 2.1 \text{ cm}^4 \quad (19)$$

where  $W_a$  is the window area of the core,  $A_e$  is the effective cross-section area of the core,  $P_o$  is the output power of the converter and  $\eta$  denotes the efficiency. From TDK datasheets, we select a proper

size of core ETD-39 ( $A_e = 1.25 \text{ cm}^2$ ,  $W_a = 2.57 \text{ cm}^2$ ,  $V_e = 11.5 \text{ cm}^3$  and  $A_L = 3150 \text{ nH/N}^2$ ) to reduce winding current density and core temperature.

By applying Faraday's law, turns ( $n_{11}$  or  $n_{22}$ ) of the coupled inductor ( $L_{11}$  or  $L_{22}$ ) can be determined as:

$$n_{11}(=n_{22}) \geq \frac{V_{i(\min)} D_{\max}}{B_{\max} A_e f_s} = 32.8 \text{ turns} \quad (20)$$

In this design,  $n_{11}$  is chosen as 35 turns. From turns ratio of the coupled inductors,  $n = (n_1 + n_{11})/n_{11}$ , the turns ( $n_1$  or  $n_2$ ) of the coupled inductance ( $L_1$  or  $L_2$ ) can be correspondingly determined as:

$$n_1(=n_2) = \frac{n_{11}}{(n-1)} = 5 \text{ (turns)} \quad (21)$$

### 5.1.2. Selection of Power Switches and Diodes

According to Equations (15) and (16), the maximum voltage stresses imposed on both free-wheeling diodes  $D_1$  and  $D_2$  is:

$$V_{D(\max)} = \frac{(V_{i(\max)} - V_o)}{n} + V_o = 35.5 \text{ V} \quad (22)$$

and both active switches  $M_1$  and  $M_2$  are:

$$V_{DS(\max)} = V_{i(\max)} + V_o(n-1) = 284 \text{ V} \quad (23)$$

When active switch  $M_1$  or  $M_2$  is turned on, the maximum switch current  $i_{DS(\max)}$  can be given as:

$$i_{DS(\max)} \approx \frac{I_o}{4} + \frac{(V_{i(\max)} - V_o) D_{\min}}{n^2 L f_s} = 9.4 \text{ A} \quad (24)$$

when free-wheeling diode  $D_1$  or  $D_2$  is conducting, the maximum diode current  $i_{D(\max)}$  can be given as

$$i_{D(\max)} \approx \frac{(V_{i(\max)} - V_o) D_{\min}}{n L f_s} = 35.4 \text{ A} \quad (25)$$

Selection of switching devices  $M_1$  and  $M_2$  involves a trade-off between conduction loss and switching loss. The selection of MOSFETs with low  $R_{ds(on)}$  will reduce conduction loss, but it will result in high parasitic capacitance. Switches with lower  $R_{ds(on)}$  also imply larger die size and higher cost. For this application, we can select the proper MOSFETs as the IRFP460, which provide high enough safety margins with a drain-source breakdown voltage of 500 V. Several important parameters of the IRFP460 are listed as follows:

$$V_{DSS} = 500 \text{ V}, R_{ds(on)} = 0.27 \Omega, C_{oss} = 870 \text{ pF} \text{ and } I_D = 20 \text{ A}$$

According to (22)~(25), with the selection of free-wheeling diodes  $D_1$  and  $D_2$ , a 40 A/60 V Schottky diode which has the lowest forward voltage drop can be employed. The Schottky diode manufactured by International Rectifier is 40CPQ60 with a maximum dc reverse voltage  $V_{RRM} = 60 \text{ V}$  and a forward voltage drop  $V_{F(\max)} = 0.47 \text{ V}$ , which is a good choice for  $D_1$  and  $D_2$ , was chosen.

5.1.3. Consideration of ZVS Condition

To achieve the ZVS feature for all of the active switches ( $M_1, M_2, M_{11}$  and  $M_{22}$ ) at turn-on transition, the IBCC is necessary to store enough energy in resonant inductor ( $L_{r1}$  or  $L_{r2}$ ). Because the voltage across main switch ( $M_1$  or  $M_2$ ) is larger than that across auxiliary switch ( $M_{11}$  or  $M_{22}$ ). Thus, the ZVS condition for all of the active switches is determined as follows:

$$L_r \geq \frac{(C_{M1} // C_{M11})(V_i - V_{cr})^2}{[I_o / 2(n-1) + \Delta i]^2} \tag{26}$$

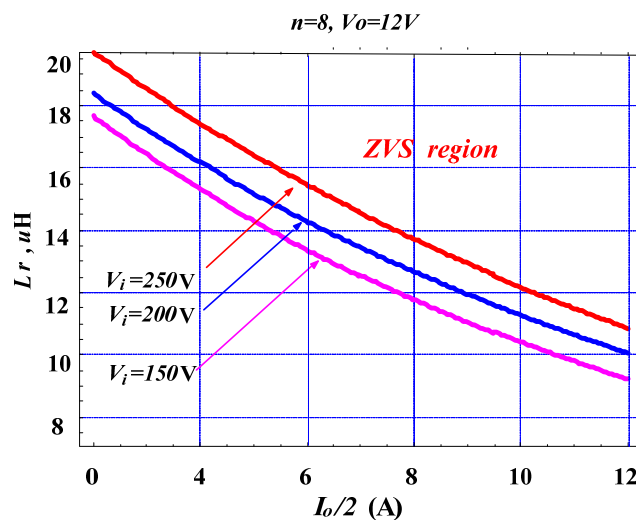
where  $\Delta i$  is the peak current of the coupled inductors, and it can be expressed as:

$$\Delta i = \frac{(n-1)(V_i - V_o)D_{max}}{nL_1f_s} \tag{27}$$

(Note: In the analysis of ZVS condition for the proposed converter, the resonant inductor is expressed as  $L_r = L_{r1} = L_{r2}$ , the clamp voltage of clamp capacitor  $V_{cr} = V_{cr1} = V_{cr2}$  and the stray capacitor of the active switch is expressed as  $C_{M1} = C_{M2}$  and  $C_{M11} = C_{M22}$ ).

According to (26), we can plot the curves showing the relationships between resonant inductor  $L_r$  and output current  $I_o$  for different values of input voltage  $V_i$ , as illustrated in Figure 13. From Figure 13, a proper value of resonant inductor  $L_r$  should be selected for achieving ZVS feature.

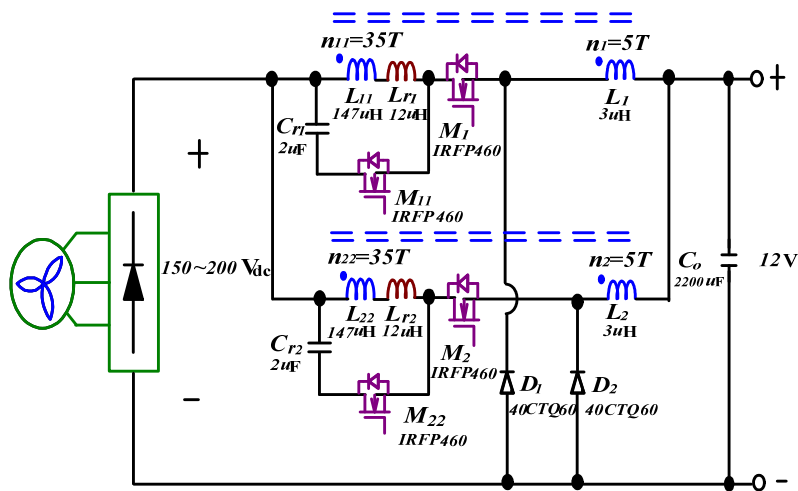
**Figure 13.** Plots of resonant inductor  $L_r$  versus output current  $I_o$  for different values of input voltage  $V_i$ .



5.2. Power Losses Estimation

Power losses of the proposed converter are estimated to verify the measured efficiency. The key component values of the experimental converter are shown in Figure 14, from which power losses are evaluated as follows:

Figure 14. Experimental circuit of the IBCC with active-clamp circuits.



### 5.2.1. Main Switches ( $M_1$ and $M_2$ )

The main switches of the proposed converter are designed to achieve ZVS during turn-on transition, so that their switching losses can be negligible. Only the conduction losses are taken into account in the estimation. Conduction losses of the main switches can be determined from their switch current  $i_{DS}$  and channel resistance  $R_{ds(on)}$ . In the proposed converter, the MOSFETs used are IRFP460, and their channel resistance  $R_{ds(on)} = 0.27 \Omega$ . In the proposed converter, the maximum duty ratio  $D_{max} = 0.41$  and switch current  $i_{DS(max)} = 9.1$  A. Thus, total power losses of the main switches can be determined as:

$$P_{Total}^{Main} = 2P_{loss(Con)}^{Main} = 2\left[\frac{1}{3}D_{max}(i_{DS(max)})^2 R_{ds(on)}\right] = \frac{2}{3}[0.41(9.1)^2(0.27)] = 6 \text{ W} \quad (28)$$

### 5.2.2. Auxiliary Switches ( $M_{11}$ and $M_{22}$ )

The auxiliary switches of the proposed converter are also designed to achieve ZVS at turn-on transitions, so that their switching losses can also be neglected. Thus, total power losses of the auxiliary switches is determined as:

$$P_{Total}^{Aux} = 2P_{loss(Con)}^{Aux} = 2\left[\frac{1}{3}(1 - D_{max})(i_{DS(max)})^2 R_{ds(on)}\right] = \frac{2}{3}[0.59(9.1)^2(0.27)] = 8.8 \text{ W} \quad (29)$$

### 5.2.3. Free-Wheeling Diodes ( $D_1$ and $D_2$ )

The free-wheeling diodes are selected as 40CPQ60 Schottky diodes, and their forward voltage drop  $V_F = 0.47$  V. Thus, total conduction losses of the free-wheeling diodes can be determined as:

$$P_{loss}^{Diode} = 2\left(\frac{I_o}{2}\right)V_F(1 - D_{max}) = 4.8 \text{ W} \quad (30)$$

### 5.2.4. Coupled Inductors ( $L_1$ and $L_2$ )

According to the datasheets of the TDK Company, the cores of the coupled inductors are designed as PC-40 ETD-39 and maximum flux  $B_{max} = 200$  mT. Their total winding turns are  $n_{total} = (n_1 + n_{11}) = 40$ ,

primary winding turns are  $n_p = n_1 = 5$ , and the turns ratio is  $n = n_{total}/n_p = 8$ . Thus, from Figure 15, we can obtain the core losses per volume,  $P_{Coup(cv)} = 0.2 \text{ W/cm}^3$  at  $60^\circ\text{C}$ . The core loss will be:

$$P_{core}^{Coup} = P_{Coup(cv)} \times V_e = 0.2 \times 11.5 = 2.3 \text{ W} \tag{31}$$

According to measurement, the winding resistance of the coupled inductors is  $R_{Coup} = 28 \text{ m}\Omega$ , and the copper losses can be estimated as:

$$P_{copper}^{Coup} = \left(\frac{I_o}{2}\right)^2 R_{Coup} = \left(\frac{20}{2}\right)^2 \times 28 \times 10^{-3} = 2.8 \text{ W} \tag{32}$$

Total power loss of the coupled inductors is therefore:

$$P_{Total}^{Coup} = 2(P_{core}^{Coup} + P_{copper}^{Coup}) = 2(2.3 + 2.8) = 10.2 \text{ W} \tag{33}$$

Power losses under full load condition on the key components are summarized in Table 1. The estimated efficiency of the proposed converter with the active-clamp circuits at input voltage  $V_i = 150 \text{ V}_{dc}$ , and full-load condition is:

$$\eta_{\%}^{\max} = \frac{P_{out}}{P_{out} + P_{loss}^{Total}} = \frac{240}{240 + 29.8} = 89\% \tag{34}$$

Figure 15. Typical core loss data of the TDK PC-40.

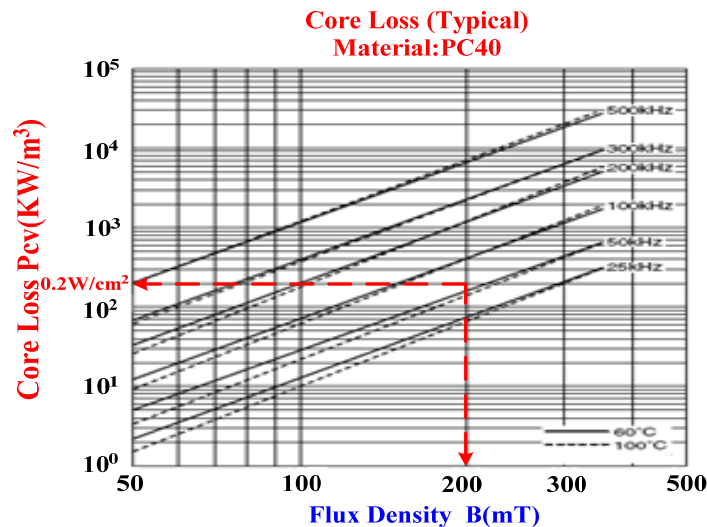


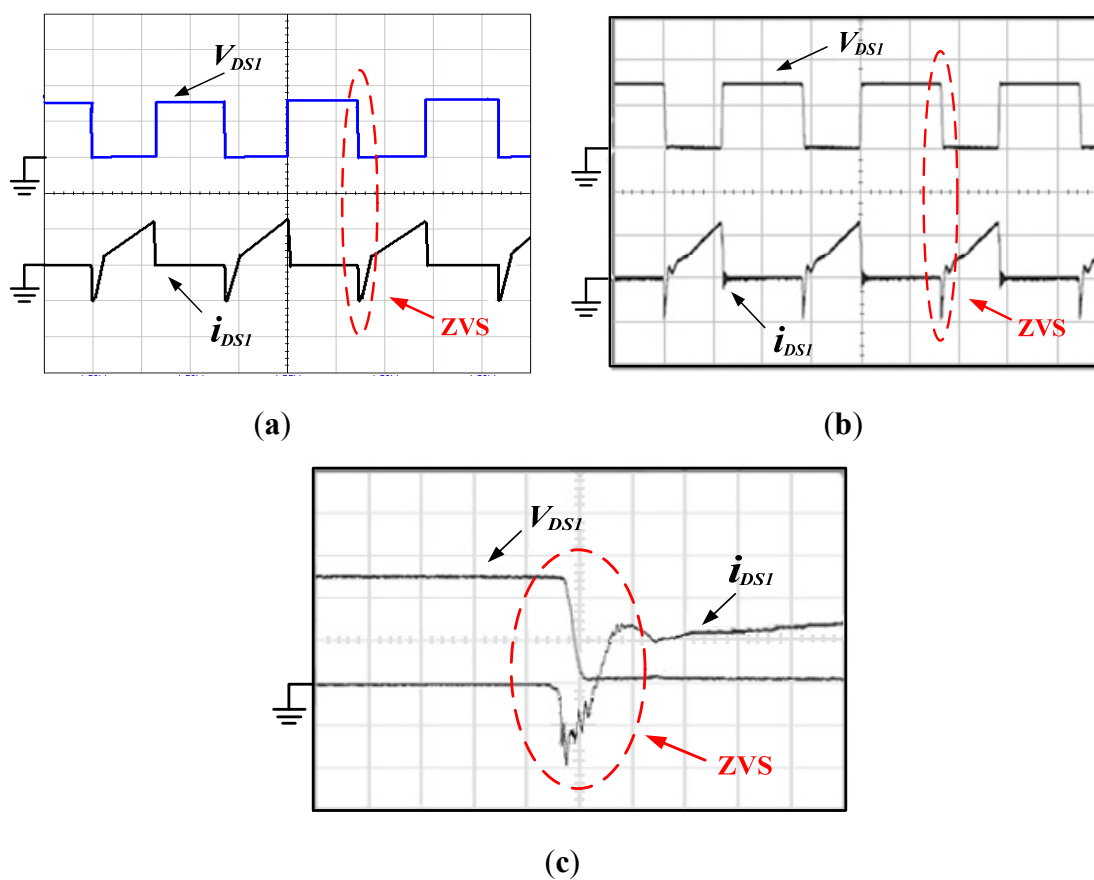
Table 1. Efficiency estimation of the proposed IBCC with active-clamp circuits.

Components	Power Loss Calculation	Power Losses
Main switch ( $M_1$ and $M_2$ )	$P_{total}^{main} = 2\left[\frac{1}{3} D_{\max} (i_{DS(\max)})^2 R_{ds(on)}\right]$	6 W
Auxiliary switch ( $M_{11}$ and $M_{22}$ )	$P_{total}^{aux} = 2\left[\frac{1}{3} (1 - D_{\max}) (i_{DS(\max)})^2 R_{ds(on)}\right]$	8.8 W
Freewheel diode ( $D_1$ and $D_2$ )	$P_{total}^{diode} = 2\left[\frac{I_o}{2} V_F (1 - D_{\max})\right]$	4.8 W
Coupled inductor ( $L_1$ and $L_2$ )	$P_{total}^{coup} = 2(P_{core}^{coup} + P_{copper}^{coup})$	10.2 W
Total power losses	$P_{Total}^{Loss} = P_{total}^{main} + P_{total}^{aux} + P_{total}^{coup}$	29.8 W
Efficiency estimation	$\eta_{\%} = \frac{P_{out}}{P_{out} + P_{Total}^{Loss}}$	89%

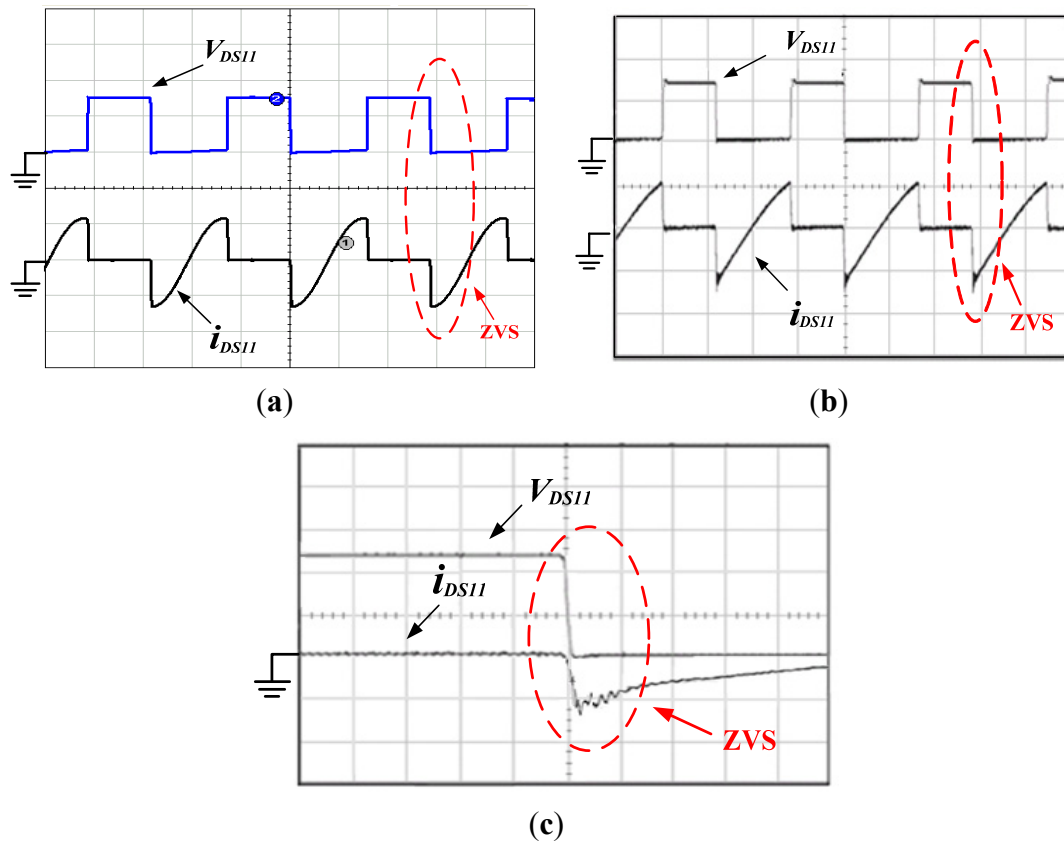
### 5.3. Experimental Results

Figure 16 shows simulated and experimental voltage and current waveforms of the main switch ( $M_1$  or  $M_2$ ), from which it can be seen that the main switch has ZVS features during the turn-on transition. Figure 17 shows simulated and experimental voltage and current waveforms of the auxiliary switch ( $M_{11}$  or  $M_{22}$ ). It can be also seen that the auxiliary switch has ZVS feature during turn-on transition. Figure 18 shows simulated and experimental inductor current waveforms of coupled inductor ( $i_{L1}$  and  $i_{L2}$ ). Figure 19 shows measured current and voltage waveforms of the free-wheeling diode ( $D_1$  or  $D_2$ ), from which it can be seen that the proposed IBCC with active-clamp circuits can limit the rate of decrease of the free-wheeling diode current, reducing reverse-recovery losses a lot. Figure 20 shows measured output voltage and current waveforms. Figure 21 shows efficiency measurements of the IBCC with active-clamp circuits, from which it can be seen that the maximum efficiency can reach as high as 91%. It can increase efficiency about 2% over the IBCC with passive-clamp circuits (as shown in Figure 3). The reason behind is that the active switches of IBCC with passive-clamp circuits are still operated in a hard-switching manner during turn-on transition.

**Figure 16.** Voltage and current waveforms of main switches ( $M_1$  or  $M_2$ ). (a) simulated results ( $V_{DS1}$ : 200 V/div;  $i_{DS1}$ : 10 A/div; Time: 5  $\mu$ s/div); (b) experimental results ( $V_{DS1}$ : 200 V/div;  $i_{DS1}$ : 10 A/div; Time: 5  $\mu$ s/div); (c) its expanded waveforms ( $V_{DS1}$ : 100 V/div;  $i_{DS1}$ : 5 A/div; Time: 0.5  $\mu$ s/div).



**Figure 17.** Voltage and current waveforms of auxiliary switch ( $M_{11}$  or  $M_{22}$ ). (a) simulated results ( $V_{DS11}$ : 200 V/div;  $i_{DS11}$ : 10 A/div; Time: 5  $\mu$ s/div); (b) experimental results ( $V_{DS11}$ : 200 V/div;  $i_{DS11}$ : 10 A/div; Time: 5  $\mu$ s/div); (c) its expanded waveforms ( $V_{DS11}$ : 100 V/div;  $i_{DS11}$ : 10 A/div; Time: 0.5  $\mu$ s/div).



**Figure 18.** Waveforms of inductor current ( $L_1$  and  $L_2$ ). (a) simulated results ( $i_{L1}$ : 10 A/div;  $i_{L2}$ : 10 A/div; Time: 5  $\mu$ s/div); (b) experimental results ( $i_{L1}$ : 10 A/div;  $i_{L2}$ : 10 A/div; Time: 5  $\mu$ s/div).

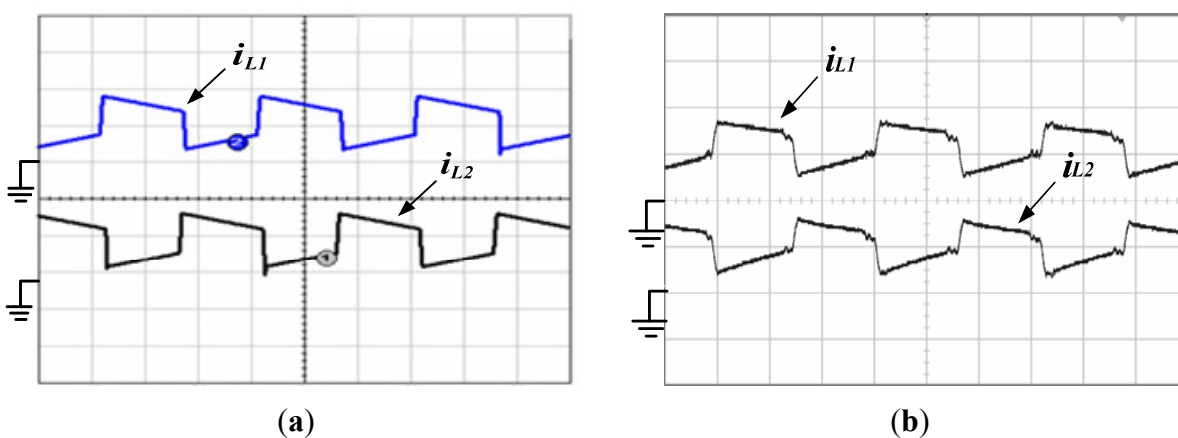


**Figure 19.** Measured voltage and current waveforms of free-wheeling diode ( $D_1$  or  $D_2$ ;  $V_{D1}$ : 20 V/div;  $i_{D1}$ : 10 A/div; Time: 200 ns/div).

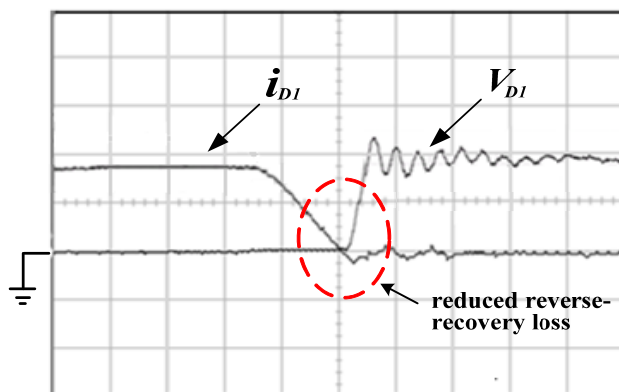


**Figure 20.** Measured output voltage and current waveforms ( $V_o$ : 5 V/div;  $I_o$ : 5 A/div; time: 500 ms/div).

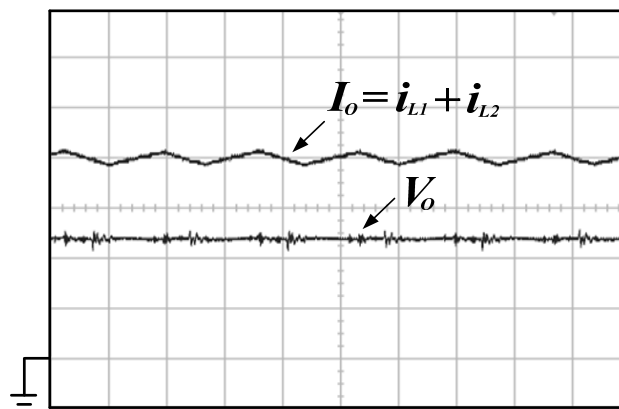
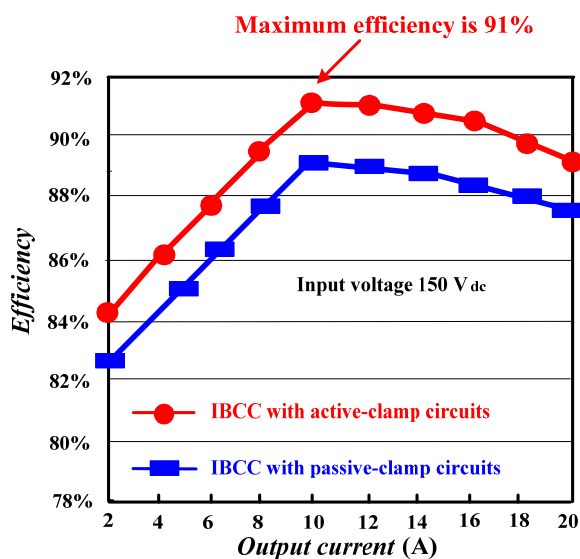


**Figure 21.** Plots of efficiency *versus* output current for the IBCC with active-clamp circuits and without active-clamp circuits at input voltage 150 V<sub>dc</sub>.



## 6. Conclusions

In this paper, an IBCC with active-clamp circuits for wind turbine conversion is proposed. The proposed converter can provide a proper duty ratio for high step-down voltage applications, resulting in low component stresses on active switches. By adopting active-clamp circuits, energy trapped in the leakage inductance of the coupled inductors can be recovered, ZVS features can be achieved and voltage spikes can be suppressed effectively for active switches. Therefore, the conversion efficiency of the proposed IBCC with active-clamp circuits can be increased significantly. In the study, analysis of the proposed IBCC with active-clamp circuits has been presented in detail, including operational principles, feature characteristics and power losses estimation. A 240 W model of the proposed IBCC with active-clamp circuits has been built and implemented. In Figure 21, experimental results can be seen showing that the maximum efficiency can reach as high as 91%. In high step-down voltage applications, the proposed IBCC with active-clamp circuits is relatively attractive for wind energy conversion.

## References

1. *World Wind Energy Report 2008*; World Wind Energy Association: Bonn, Germany, 2009.
2. Rahimi, M.; Parniani, M. Efficient control scheme of wind turbines with doubly fed induction generators for low-voltage ride-through capability enhancement. *Renew. Power Gener. IET* **2010**, *4*, 242–252.
3. Tsai, C.T. Energy storage system with voltage equalization strategy for wind conversion. *Energies* **2012**, *5*, 2331–2350.
4. Shen, C.L.; Tsai, C.T. Double-linear approximation algorithm to achieve maximum-power-point tracking for photovoltaic arrays. *Energies* **2012**, *5*, 1982–1997.
5. Agarwal, V.; Aggarwal, R.K.; Patidar, P.; Patki, C. A novel scheme for rapid tracking of maximum power point in wind energy generation systems. *IEEE Trans. Power Electron.* **2010**, *25*, 228–236.
6. Wong, P.; Xu, P.; Lee, F.C. Performance improvements of interleaving VRMs with coupling inductors. *IEEE Trans. Power Electron.* **2001**, *16*, 499–507.
7. Chen, Y.M.; Tseng, S.Y.; Tsai, C.T.; Wu, T.F. Interleaved buck converters with a single-capacitor turn-off snubber. *IEEE Trans. Aerosp. Electron. Syst.* **2004**, *40*, 954–967.
8. Munoz, C. Study of a New Passive Lossless Turn-Off Snubber. In *Proceedings of the International Power Electronics Congress*, Seoul, Korea, 26–31 October 1998; pp. 147–152.
9. Smith, K.M., Jr.; Smedley, K.M. Lossless Passive Soft Switching Methods for Inverters and Amplifiers. In *Proceedings of the Power Electronics Specialists Conference*, Saint Louis, MO, USA, 22–27 June 1997; pp. 1431–1439.
10. Ilic, M.; Maksimovic, D. Interleaved zero-current-transition buck converter. *IEEE Trans. Ind. Appl.* **2007**, *43*, 1619–1627.
11. Tseng, C.J.; Chen, C.L. Passive Lossless Snubbers for DC/DC Converters. *IEE Proc. Circuits Device Syst.* **1998**, *145*, 396–401.

12. Gallo, C.A.; Tofoli, F.L.; Pinto, J.A.C. A passive lossless snubber applied to the AC-DC interleaved boost converter. *IEEE Trans. Power Electron.* **2010**, *25*, 775–785.
13. Tsai, C.T.; Shen, C.L. Interleaved soft-switching buck converter with coupled inductors. *WSEAS Trans. Circuits Syst.* **2011**, *10*, 99–103.
14. Yao, K.; Ye, M.; Xu, M.; Lee, F.C. Tapped-inductor buck converter for high-step-down DC-DC converter. *IEEE Trans. Power Electron.* **2005**, *20*, 775–780.
15. Shoyama, M.; Li, G.; Ninomiya, T. Application of Common-Source Active-Clamp Circuit to Various DC-DC Converter Topologies. In *Proceedings of the Power Electronics Specialists Conference*, Acapulco, Mexico, 15–19 June 2003; pp. 1321–1326.
16. Xu, D.H.; Chen, M.; Lou, J.; Luo, M. Transformer secondary leakage inductance based ZVS dual bridge DC/DC converter. *IEEE Trans. Power Electron.* **2004**, *19*, 1408–1416.
17. Jin, K.; Ruan, X. Zero-voltage-switched multi-resonant three-level converters. *IEEE Trans. Ind. Electron.* **2007**, *54*, 1705–1715.
18. Lo, Y.K.; Kao, T.S.; Lin, J.K. Analysis and design of an interleaved active-clamp forward converter. *IEEE Trans. Ind. Electron.* **2007**, *54*, 2323–2332.

© 2012 by the authors; licensee MDPI, Basel, Switzerland. This article is an open access article distributed under the terms and conditions of the Creative Commons Attribution license (<http://creativecommons.org/licenses/by/3.0/>).